

**Climatology, seasonality and trends of oceanic coherent  
eddies**

**Josué Martínez-Moreno<sup>1</sup>, Andrew McC. Hogg<sup>1</sup>, and Matthew H. England<sup>2</sup>**

<sup>4</sup> Research School of Earth Science and ARC Center of Excellence for Climate Extremes, Australian  
<sup>5</sup> National University, Canberra, Australia

<sup>6</sup> Climate Change Research Centre (CCRC), UNSW Australia, Sydney NSW, Australia

**Key Points:**

- <sup>8</sup> Kinetic energy of coherent eddies contain around 50% of the surface ocean kinetic  
<sup>9</sup> energy budget.
- <sup>10</sup> Seasonal cycle of the number of coherent eddies and coherent eddy amplitude re-  
<sup>11</sup> veal a 3-6 month lag to wind forcing
- <sup>12</sup> Inverse cascade sets up the seasonal lag of the number and amplitude of coher-  
<sup>13</sup> ent eddies.
- <sup>14</sup> The coherent eddy amplitude has increase at a rate of 3 cm per decade since 1993.

---

Corresponding author: Josué Martínez-Moreno, [josue.martinezmoreno@anu.edu.au](mailto:josue.martinezmoreno@anu.edu.au)

15 **Abstract**

Ocean eddies influence regional and global climate through mixing and transport of heat and properties. One of the most recognizable and ubiquitous feature of oceanic eddies are vortices with spatial scales of tens to hundreds of kilometers, frequently referred as “mesoscale eddies” or “coherent eddies”. Coherent eddies are known to transport properties across the ocean and to locally affect near-surface wind, cloud properties and rainfall patterns. Although coherent eddies are ubiquitous, yet their climatology, seasonality and long-term temporal evolution remains poorly understood. Thus, we examine the kinetic energy contained by coherent eddies and we present the annual and long-term changes of automatically identified coherent eddies from satellite observations from 1993 to 2018. Around 50% of the kinetic energy contained by ocean eddies corresponds to coherent eddies. Additionally, a strong hemispherical seasonal cycle is observed, with a 3–6 months lag between the wind forcing and the response of the coherent eddy field. Furthermore, the seasonality of the number of coherent eddies and their amplitude reveals that the number of coherent eddies responds faster to the forcing ( $\sim 3$  months), then the coherent eddy amplitude (which is lagged by  $\sim 6$  months). Our analysis highlights the relative importance of the coherent eddy field in the ocean kinetic energy budget, implies a strong response of the eddy number and eddy amplitude to forcing at different time-scales, and showcases the seasonality, and multidecadal trends of coherent eddy properties.

35 **Plain language summary**36 **1 Introduction**

Mesoscale ocean variability with spatial scales of tens to hundreds of kilometers is comprised of processes such as vortices, waves, and jets (Ferrari & Wunsch, 2009; Fu et al., 2010). These mesoscale processes are highly energetic, and they play a crucial role in the transport of heat, salt, momentum, and other tracers through the ocean (Wunsch & Ferrari, 2004; Wyrtki et al., 1976; Gill et al., 1974). Possibly, the most recognizable and abundant process observed from satellites is mesoscale vortices. Although mesoscale vortices are commonly referred to in literature as “mesoscale eddies”, this term is also often used to describe the total mesoscale ocean variability (the time-varying component of the mesoscale flow), thus, here we will refer to mesoscale vortices as *coherent eddies*.

46 Coherent eddies are quasi-circular currents. According to their rotational direction,  
47 the sea surface height anomaly within a coherent eddy can have a negative or positive  
48 sea surface height anomaly (cold-core and warm-core coherent eddies, respectively). This  
49 characteristic sea surface height signature of coherent eddies has been utilized to auto-  
50 matically identify and track coherent eddies from satellite altimetry (Cui et al., 2020;  
51 Martínez-Moreno et al., 2019; Ashkezari et al., 2016; Faghmous et al., 2015; Chelton et  
52 al., 2007). Automated identification algorithms of coherent eddies have shown their ubiq-  
53 uituity in the oceans, with a predominant influence at hotspots of eddy activity such as bound-  
54 ary currents and the Antarctic Circumpolar Current. In these regions, Chelton et al. (2011)  
55 estimated that coherent eddies contribute around 40–50% of the mesoscale kinetic en-  
56 ergy (Chelton et al., 2011) and thus a significant fraction of the total kinetic energy (Fer-  
57 rari & Wunsch, 2009). Although this unique estimate showcases the importance of the  
58 mesoscale coherent eddy field, the energy contained by coherent eddies was estimated  
59 by extracting the geostrophic velocities within the detected coherent eddies, thus it is  
60 possible it may contain energy from other processes. Coherent eddies are not only abun-  
61 dant and may have a large proportion of the surface kinetic energy budget, but they are  
62 also essential to ocean dynamics as concluded by many previous studies (Patel et al., 2020;  
63 Schubert et al., 2019; Pilo et al., 2015; Frenger et al., 2015, 2013; Beron-Vera et al., 2013;  
64 Siegel et al., 2011; Hogg & Blundell, 2006).

65 There is broad consensus that mesoscale eddy kinetic energy has a pronounced sea-  
66 sonal variability (Uchida et al., 2017; Kang & Curchitser, 2017; Qiu & Chen, 2004; Qiu,  
67 1999). Several hypotheses have been proposed to explain this seasonality including: sea-  
68 sonal variations of atmospheric forcing (Sasaki et al., 2014), seasonality of the mixed layer  
69 depth (Qiu et al., 2014; Callies et al., 2015), seasonality of the intensity of barotropic in-  
70 stability (Qiu & Chen, 2004), the variability of the baroclinic instability due to the sea-  
71 sonality of the vertical shear (Qiu, 1999), and a seasonal lag of the inverse energy cas-  
72 cade (energy is transported between scales from small to large; Arbic et al., 2013) in com-  
73 bination with the presence of a front in the mixed layer, which can lead to a seasonal  
74 cycle of the baroclinic instability (Qiu et al., 2014). On one hand, processes such as barotropic  
75 and baroclinic instabilities control the seasonality of coherent eddies in the ocean. On  
76 the other hand, recent studies using observations and eddy-permitting climate models  
77 suggest several long-term adjustments of the global ocean capable of long-term changes  
78 in the coherent eddy field. Such readjustments include a multidecadal increase in the ocean

stratification resulted from temperature and salinity changes (Li et al., 2020), a horizontal readjustment of the sea surface temperature gradients (Ruela et al., 2020; Bouali et al., 2017; Cane et al., 1997), and an intensification of the kinetic energy, eddy kinetic energy, and mesoscale eddy kinetic energy over the last 3 decades as a consequence of an increase in wind forcing (Hu et al., 2020; Wunsch, 2020; Martínez-Moreno et al., 2021). All these seasonal factors and long-term readjustments directly influence the annual and decadal response of the coherent eddy field, however, the seasonality of the coherent component of the eddy kinetic energy, as well as the seasonal cycle and trends of the coherent eddy statistics remain unknown.

Here we present a new global climatology of the coherent eddy kinetic energy by reconstructing the coherent eddy signature from satellite observations. Our climatology documents the seasonal cycle of the coherent eddy kinetic energy, and seasonal cycle and long-term trends of the coherent eddy properties over the satellite record. Moreover, we conduct more detail analysis in regions where coherent eddies dominate the eddy kinetic energy field. This paper is structured as follows: the data sources and methodology are described in section 2. Then, we present the climatology, energy ratios, and global seasonality of the coherent eddy kinetic energy in subsection 3. Subsection 4 presents the global climatology and seasonality of coherent eddy properties, followed by the seasonal cycle and coherent eddy property time-series in regions dominated by coherent eddies (subsection 6). We then focus our attention on the long-term changes of the coherent eddy properties (section 5). Finally, section 7 summarizes the main results and discusses the implications of this study.

## 2 Methods

We use daily sea surface height (SSH) data made available by the Copernicus Marine Environment Monitoring Service in near real time (CMEMS, 2017). This gridded product contains the sea surface height and geostrophic velocities with daily  $0.25^\circ$  resolution from January 1993 to 2019. The daily geostrophic velocities allowed us to compute the kinetic energy (KE) and eddy kinetic energy (EKE) over the satellite record. The main source of EKE is the time-varying wind (Ferrari & Wunsch, 2009), thus we computed the seasonal cycle of the wind magnitude from the JRA55 reanalysis (Japan Meteorological Agency, Japan, 2013) using wind velocities at 10m above the ocean's surface.

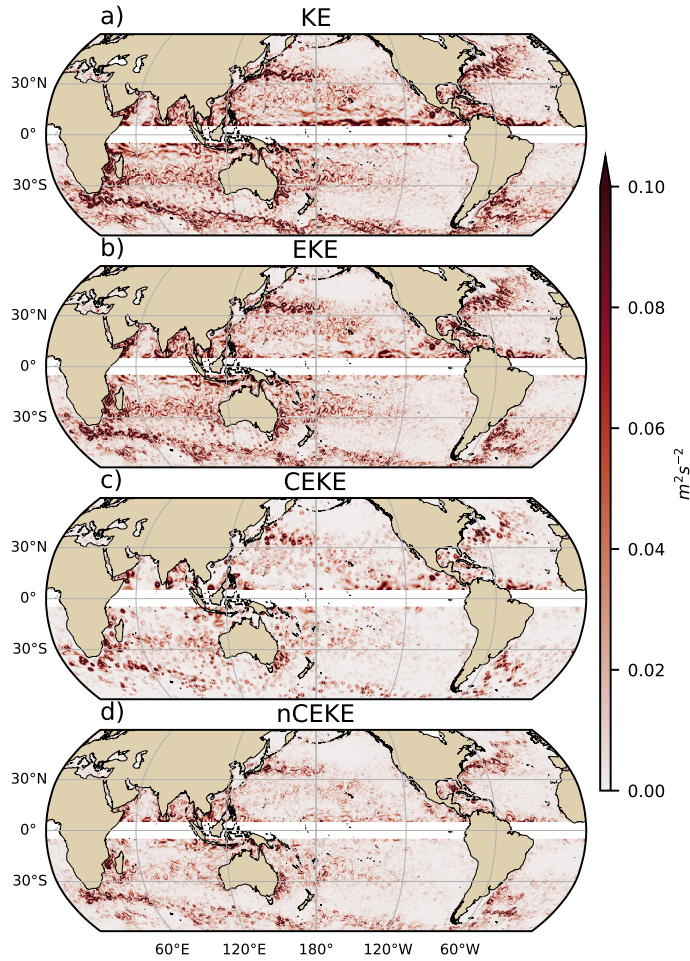
Over the same record, coherent eddy statistics from Martínez-Moreno et al. (2019), hereafter M-M, are analyzed and compared to those released by Chelton & Schlax (2013), both datasets are gridded in a  $1^\circ$  resolution. Although both datasets are produced via automated eddy identification algorithms using closed contours of SSH, these datasets have important differences in the criteria they use to identify and record coherent eddies statistics. The major difference include; (i) M-M's algorithm requires an adjustment between a 2D Gaussian and the SSH anomaly (SSHa) surface within the identify closed contour, while Chelton's only uses the outer-most closed contour of SSH; (ii) M-M's dataset reports the maximum SSHa within the identified coherent eddy, while Chelton's algorithm reports the maximum SSH value minus the discrete level in which the coherent eddy was identified; M-M's dataset includes all detected coherent eddies, while Chelton's dataset excludes (iii) coherent eddies with lifetimes shorter than four weeks and (iv) coherent eddy amplitudes smaller than 1cm. Moreover, M-M's algorithm allows the reconstruction of the coherent eddy field under the assumption that coherent eddies have a 2D Gaussian imprint in the sea surface height. These Gaussian anomalies then allow us to estimate the coherent geostrophic eddy velocities and thus the kinetic energy contained only by coherent eddies.

## 2.1 Kinetic Energy decomposition

Kinetic energy is commonly divided into the mean and time-varying components through a Reynolds decomposition. At a given time, the velocity field  $\mathbf{u} = (u, v)$  is split into the time mean ( $\bar{\mathbf{u}}$ ) and time varying components ( $\mathbf{u}'$ ). Moreover, M-M proposed to further decompose the eddy kinetic energy into the energy contained by coherent features ( $\mathbf{u}'_e$ ) and non-coherent features ( $\mathbf{u}'_n$ ). Therefore the KE equation can be written as:

$$\text{KE} = \underbrace{\bar{u}^2 + \bar{v}^2}_{\text{MKE}} + \underbrace{u'^2_e + v'^2_e + u'^2_n + v'^2_n}_{\text{CEKE}} + \underbrace{\mathcal{O}_c^2}_{\text{nCEKE}} + \mathcal{O}^2 \quad (1)$$

Due to the properties of this decomposition, the second order term  $\mathcal{O}^2$  is zero when averaged over the same period as  $\bar{\mathbf{u}}$ . However,  $\mathcal{O}_c^2$  is negligible when averaged over time and space. More information about the decomposition of the field into coherent features and non-coherent features is explained by Martínez-Moreno et al. (2019). A global snap-



144 **Figure 1.** Snapshot of surface kinetic energy ( $\overline{KE}$ ), surface eddy kinetic energy ( $\overline{EKE}$ ),  
 145 surface coherent eddy kinetic energy ( $\overline{CEKE}$ ), and surface non-coherent eddy kinetic energy  
 146 ( $\overline{nCEKE}$ ) for the 1st of January 2017.

139 shot of each component of kinetic energy decomposition is shown in Figure 1, where the  
 140 KE and EKE are comprised of rings and filaments. As expected, the decomposition of  
 141 EKE into CEKE and nCEKE components exhibit only ring-like signatures expected of  
 142 coherent eddies, while the non-coherent component shows filaments and some uniden-  
 143 tified coherent eddies.

## 147 2.2 Eddy statistics

148 The eddy statistics used in this study include the eddy count ( $cEddy_n$ ) defined as  
 149 the number of eddies per grid cell, and the mean eddy amplitude defined as the mean

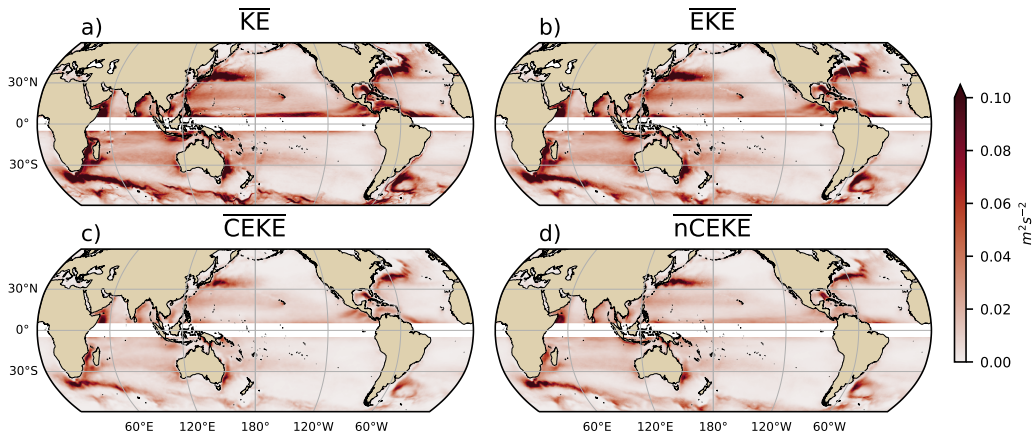
150 amplitude of the coherent eddies within the cell ( $cEddy_{amp}$ ), The latter metric can be  
 151 separated into positive ( $cEddy_{amp}^+$ ) and negative ( $cEddy_{amp}^-$ ) coherent eddy amplitudes,  
 152 defined as the mean amplitude of warm core and cold core coherent eddies, respectively,  
 153 within the cell. The absolute eddy amplitude ( $|cEddy_{amp}|$ ) is then defined as:

$$|cEddy_{amp}| = \frac{1}{2} (cEddy_{amp}^+ - cEddy_{amp}^-) \quad (2)$$

154 Note that the  $cEddy_{amp}^+$  and  $cEddy_{amp}^-$  are sign definite, thus the difference will always  
 155 be positive, mean  $cEddy_{amp}$  can be negative or positive noting the dominant polarity  
 156 of coherent eddies in the region. We analyze the climatology, seasonal cycles and trends  
 157 of the eddy statistics between 1993 and 2019. We exclude the equatorial region ( $10^\circ S$   
 158 -  $10^\circ N$ ) and poleward of  $60^\circ$ . Note that the climatology of  $cEddy_n$  is computed by adding  
 159 all the identified eddies over the record, while all other climatological statistics are com-  
 160 puted as the time-average over the record. Seasonal climatologies are calculated for the  
 161 monthly average of each coherent eddy statistic, while hemispherical time-series are fil-  
 162 tered with a running average of 90 days. Trends of  $cEddy_n$  and  $|cEddy_{amp}|$  are calcu-  
 163 lated by coarsening the dataset to a  $5^\circ$  grid, and then linear trends are computed for each  
 164 grid point, the statistical significance is assessed by a modified Mann-Kendall test (Yue  
 165 & Wang, 2004). Time averages are denoted by  $\overline{\cdot}$ , while area averages are shown by  $\langle \cdot \rangle$ .

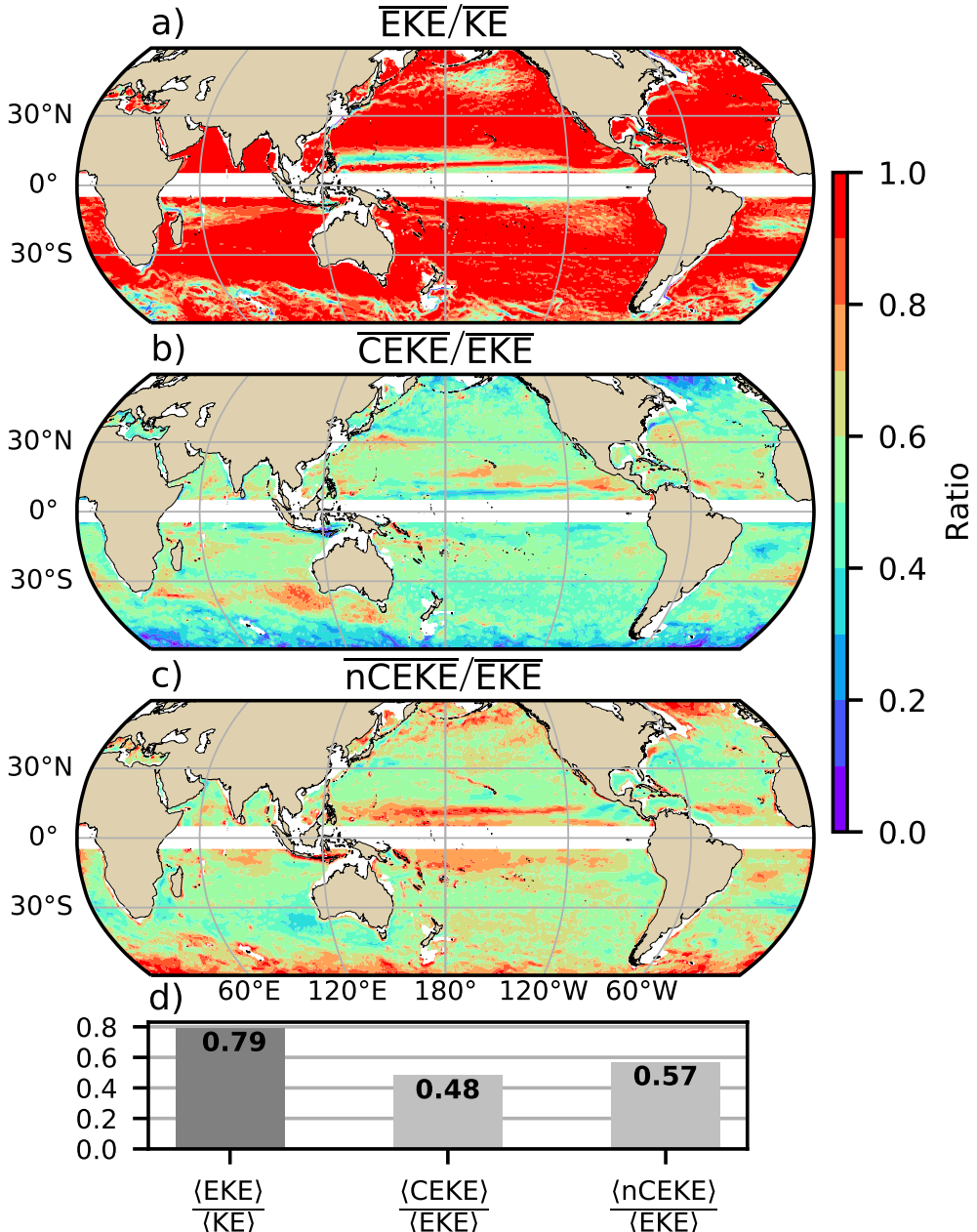
### 166 3 Global Coherent Eddy Energetics

167 The climatology geostrophic components of the kinetic energy decomposition es-  
 168 timated from sea surface height are shown in Figure 2. These maps show that many re-  
 169 gions of the global ocean are highly energetic in mean KE ( $\overline{KE}$ ), mean EKE ( $\overline{EKE}$ ), mean  
 170 coherent eddy kinetic energy ( $\overline{CEKE}$ ) and mean non-coherent eddy kinetic energy ( $\overline{nCEKE}$ ).  
 171 The spatial pattern highlights well known regions of the ocean, where mesoscale processes  
 172 are abundant, such is the case of western boundary currents, the Antarctic Circumpo-  
 173 lar Current and regions within the ocean gyres. Remarkably, the spatial distribution of  
 174 the energy contained by the reconstructed mesoscale coherent eddies and non-coherent  
 175 components are similar (Figures 2c,d), which can be thought as regions where mesoscale  
 176 activity is intense, however, there are some regions where coherent eddies dominate over  
 177 non-coherent and vice-versa. Overall, this decomposition suggest that boundary currents  
 178 and other energetic regions, in particular, eddy-rich regions in the ocean contain both  
 179 coherent and non-coherent components of the kinetic energy.



180      **Figure 2.** Climatology of surface kinetic energy ( $\overline{KE}$ ), surface eddy kinetic energy ( $\overline{EKE}$ ),  
 181      surface coherent eddy kinetic energy ( $\overline{CEKE}$ ), and surface non-coherent eddy kinetic energy  
 182      ( $\overline{nCEKE}$ ) between 1993-2018.

192      Eddy kinetic energy is known to be more than an order of magnitude greater than  
 193      MKE (Gill et al., 1974), this is clearly shown in Figure 3a, where the ratio of  $\overline{EKE}$  is re-  
 194      sponsible of almost all the  $\overline{KE}$  across the ocean, except for regions with persistent cur-  
 195      rents over time. Such regions are located in the mean boundary current locations, the  
 196      equatorial pacific currents and regions in the Antarctic Circumpolar current, where the  
 197      EKE explains around 40% of the  $\overline{KE}$ . As estimated by a previous study by Chelton et  
 198      al. (2011), the EKE within coherent eddies with lifetimes greater than 4 weeks contain  
 199      between 40 to 60 percent of the  $\overline{EKE}$ . Our result from reconstructing the coherent eddy  
 200      signature (Figure 3b) further corroborates that the coherent component ( $\overline{CEKE}$ ) has around  
 201      50% of the  $\overline{KE}$  (Figure 3d). Furthermore, global averages of the ratios show  $\overline{EKE}$  ex-  
 202      plains approximately 78% of the ocean  $\overline{KE}$  field, while non coherent eddy features con-  
 203      tain 48% and 57% percent. Note the globally averaged coherent and non coherent com-  
 204      ponents do not add to 100% as the cross terms ( $O_c^2$ ) are different to zero. This is likely  
 205      to errors in the coherent eddy reconstruction. The spatial pattern reveals a dominance  
 206      of the  $\overline{CEKE}$  equatorward from the boundary currents and areas with large coherent eddy  
 207      contributions of around 90% of the region's eddy kinetic energy, for example, south of  
 208      Australia, Tehuantepec Gulf and South Atlantic. An evident signal is an reduction of  
 209      the energy contained by coherent eddies at high latitudes and an increase in the energy  
 210      explained by non-coherent eddies, this could be a consequence of the incapability of the



183 **Figure 3.** Ratios of the kinetic energy components. a) Map of the proportion of mean eddy  
 184 kinetic energy (EKE) versus mean kinetic energy ( $\bar{KE}$ ); b) Map of the percentage of mean co-  
 185 herent eddy kinetic energy ( $\bar{CEKE}$ ) versus mean eddy kinetic energy ( $\bar{EKE}$ ); c) Map of the  
 186 percentage of mean non-coherent eddy kinetic energy ( $\bar{nCEKE}$ ) versus mean eddy kinetic en-  
 187 ergy ( $\bar{EKE}$ ); d) Global area averaged percentage of mean eddy kinetic energy ( $\langle EKE \rangle$ ) versus  
 188 the global mean kinetic energy ( $\langle \bar{KE} \rangle$ ), area averaged percentage of mean coherent eddy kinetic  
 189 energy ( $\langle \bar{CEKE} \rangle$ ) and mean non coherent eddy kinetic energy ( $\langle \bar{nCEKE} \rangle$ ) versus global mean  
 190 eddy kinetic energy ( $\langle \bar{EKE} \rangle$ ). Regions where the depth of the ocean is shallower than 1000m are  
 191 removed from the ratio estimation.

211 0.25° satellite resolution ( $\sim 13$  km at 60°) to fully resolve coherent eddies with scales  
 212 smaller than  $\sim 10$  km (first baroclinic Rossby radius at 60°)

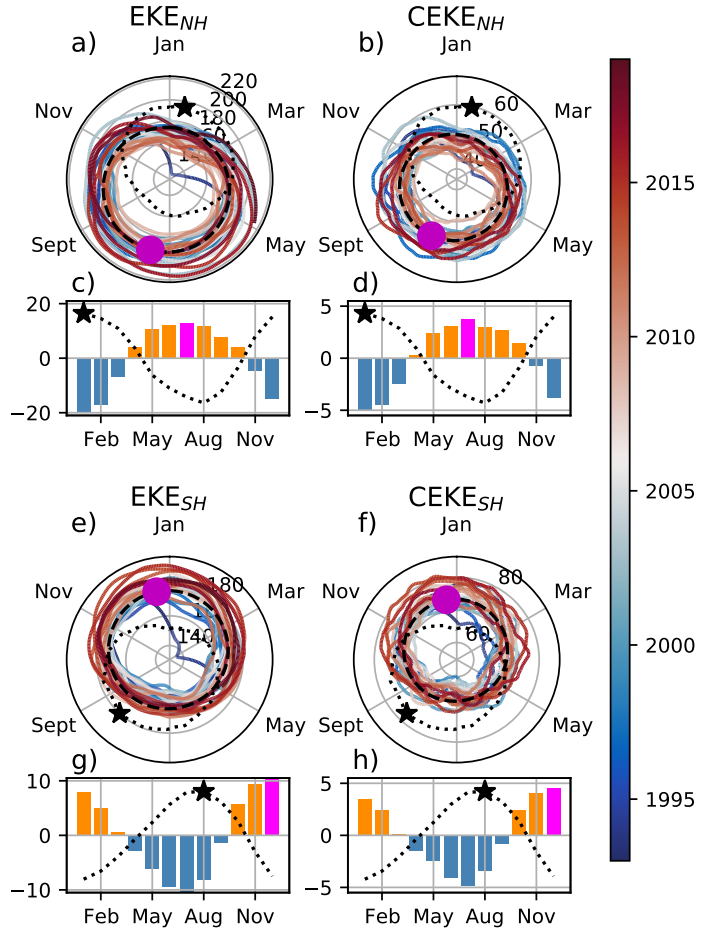
213 ***3.0.1 Seasonality***

214 In accordance with the previously observed EKE seasonal cycle, we investigate sea-  
 215 sonal cycle of the EKE and CEKE for the northern hemisphere (NH; 10°N - 60°N) and  
 216 Southern Hemisphere (SH; 60°S - 10°S). In both hemispheres (Figure 4), the EKE and  
 217 CEKE peak during the hemispherical summer. In the northern hemisphere, the largest  
 218 EKE and CEKE occurs  $\sim 6$  months after the maximum winds (Figure 4c and d), while  
 219 the Southern ocean seems to respond within  $\sim 4$  months (Figure 4g, and h). This sea-  
 220 sonal lag and maximum is consistent with a time-lag of the inverse cascade (Sasaki et  
 221 al., 2014; Qiu et al., 2014) where winter has the highest energy at the smallest scales (non-  
 222 solvable with satellite observations), spring and autumn have the highest and lowest en-  
 223 ergy in scales of 50-100 km, and summertime has the highest energy at the largest scales  
 224 ( $> 100$  km; Uchida et al. 2017), thus the maximum of EKE and CEKE located during  
 225 summertime suggest eddies and coherent eddies have scales larger than 100 km.

226 The cyclic plots in Figure 4 shows the temporal evolution of EKE and CEKE. Note  
 227 that high frequency variability can be observed in the CEKE field with temporal scales  
 228 of a few months, this could be attributed local dynamics averaged over the hemisphere,  
 229 as well as errors within the coherent eddy identification. Additionally, cyclic plots high-  
 230 light long-term temporal changes over the record; (i) northern hemisphere winters show  
 231 a decrease in the CEKE field and (ii) the Southern hemisphere show concentric growth  
 232 over time in EKE and CEKE, which support the increasing trends in the Southern Ocean  
 233 observed by (Hogg et al., 2015; Martínez-Moreno et al., 2019; Martínez-Moreno et al.,  
 234 2021).

241 **4 Global Coherent Eddy Statistics**

242 Identified coherent eddies properties using automated algorithms allows to estimate  
 243 the contribution and temporal changes in the number of eddies and the eddy amplitude.  
 244 Figure 5 shows gridded global coherent eddy statistics; the number of eddies and eddy  
 245 amplitude. We checked M-M eddy count against Chelton et al. (2007) (Figure 5a-b). Al-  
 246 though the number of the identified eddies is larger in M-M, possibly due to the lifes-



235 **Figure 4.** Hemispherical seasonality of eddy kinetic energy (EKE), coherent eddy kinetic en-  
 236 ergy (CEKE). Panels a, and b show the northern hemisphere seasonal cycle, while panels c, and  
 237 d correspond to the southern hemisphere. Dashed lines correspond to the seasonal cycle of the  
 238 fields and dotted lines show the seasonal cycle of the wind magnitude smoothed over 120 days  
 239 (moving average). The green and magenta stars show the maximum of the seasonal cycle for the  
 240 kinetic energy components and the wind magnitude, respectively. The line colors show the year.

pan filter implemented by Chelton. Overall both datasets reveal consistent spatial patterns, for example, both datasets show high abundance of eddies in the East North Pacific, East North Atlantic, as well as the East South Pacific, East South Atlantic and East Indian Ocean, and small number counts of eddies in the tropics and at high latitudes. An interesting pattern emerges in both eddy count datasets, where clusters with larger eddy counts are favored across the ocean, in addition to coherent eddy propagation patterns in boundary currents and regions in the Southern Ocean. Furthermore, these clusters of coherent eddies could be associated with topographic features, however it remains puzzling the consistency of the eddy count pattern.

Regions with large counts of eddies have small absolute amplitudes (Figure 5 c), while regions such as the boundary currents and Antarctic Circumpolar Current have the largest coherent eddy absolute amplitudes as shown by Chelton et al. (2011), followed by the interior of ocean gyres. Note that eddy amplitude highlights regions dominated by particular coherent eddy polarity, for example, boundary currents have a preferred sign (Figure 5 d); positive amplitude polewards to the boundary current mean location, and negative amplitude equatorwards. This sign preference is consistent with way coherent eddies are shed from boundary currents. These global statistics reveal the absolute coherent eddy amplitude is a proxy of the CEKE with similar spatial patterns (Figure 2 & Figure 5 c) and showcases that regions where  $\overline{\text{CEKE}}$  has a large proportion of the  $\overline{\text{EKE}}$  (Figure 3), the absolute coherent eddy amplitude is also large.

#### 4.0.1 Seasonality

To further understand the seasonal cycle of CEKE, we compute hemispherical seasonality of the coherent eddy properties (Figure 6). The seasonality of the number of eddies in the Northern Hemisphere peaks on April (Figure 6a,c), while the Southern Hemisphere maximum number of eddies is around October (Figure 6e,g). Meanwhile, the seasonality of the absolute eddy amplitude peaks in August and January for the Northern and Southern Hemispheres respectively (Figure 6b,d,f, and h). As expected, the seasonality of the absolute eddy amplitude or intensity of the coherent eddies is consistent with the seasonal cycle of CEKE. Furthermore, a distinct lag of  $\sim 3$  months is observed between the forcing (winds) and eddy count, while the eddy amplitude maximum occurs  $\sim 6$  months after the seasonal maxima in winds. This lag suggest the eddy number increases earlier in the year and through eddy-eddy interactions (merging of coherent ed-

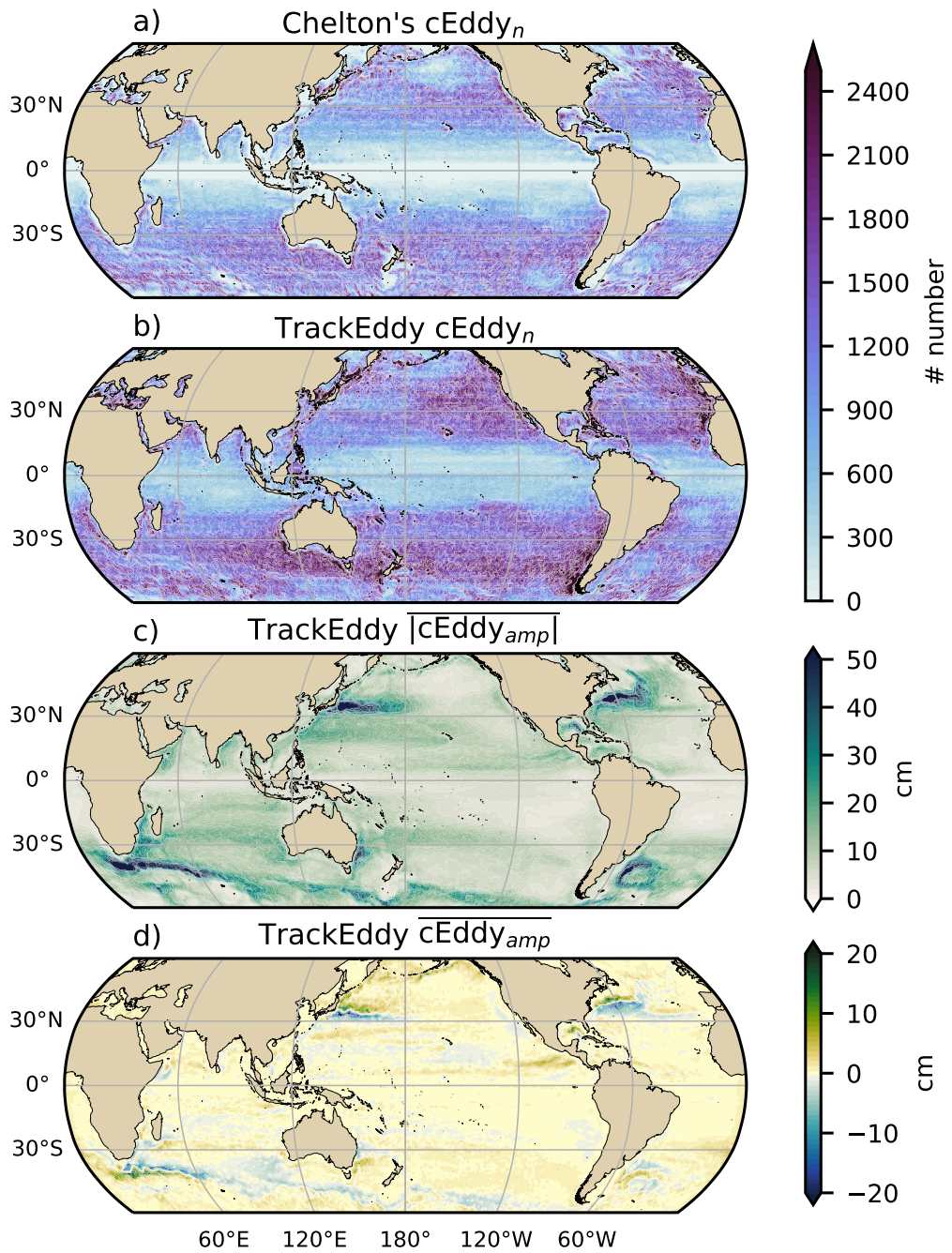


**Figure 5.** Climatology of the coherent eddy statistics. a) Climatology of the number of coherent eddies ( $cEddy_n$ ) identified by Chelton et al. (2007); b) Climatology of the number of coherent eddies ( $cEddy_n$ ) identified by Martínez-Moreno et al. (2019); c) Climatology of the mean absolute coherent eddy amplitude ( $cEddy_{amp}$ ). d) Climatology of the mean coherent eddy amplitude ( $cEddy_{amp}$ ).

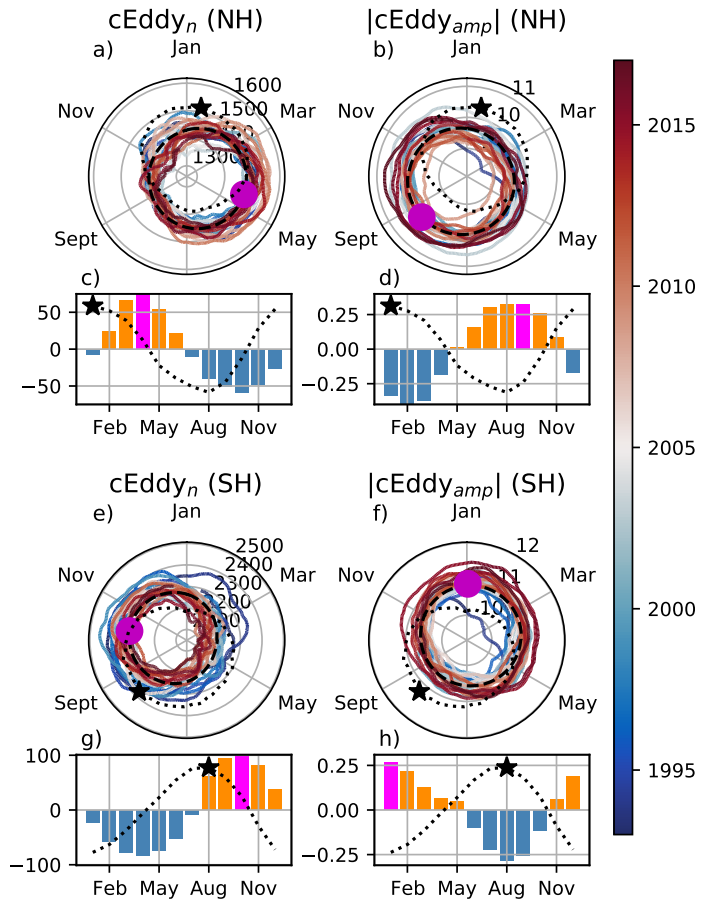
284 dies) the amplitude of the coherent eddy increases. This can be further explored by looking  
 285 at the eddy diameter. Note that 90% of identified eddies have diameters between 50  
 286 to 220 km (Figure 7a), but more importantly, we observe in the Northern Hemisphere  
 287 large-scale coherent eddies (diameter > 120 km) maximum diameter occur during Septem-  
 288 ber, while small-scale coherent eddies (diameter < 120 km) seasonal peak is during May  
 289 (Figure 7b). Meanwhile, in the Southern Hemisphere, the large-scale coherent eddies oc-  
 290 curs in February, while the small-scale coherent eddies peak in December (Figure 7c).  
 291 This result is consistent with baroclinic instabilities generating many small coherent ed-  
 292 dies early, which then are capable to merge and grow to become larger and more ener-  
 293 getic. This process can be thought analogous to the inverse energy cascade, thus this mech-  
 294 anism not only drives the EKE seasonality, but also the seasonal cycle of coherent ed-  
 295 dies.

296 Long-term changes can be observed in Figure 6a,b, e, and f where growing-shrinking  
 297 concentric circles over time denote an increase-decrease trend of the field. This is par-  
 298 ticularly evident in the Southern Hemisphere, where the number of eddies has decreased,  
 299 the eddy amplitude has increased. This result is consistent with the observed trends in  
 300 EKE and mesoscale EKE in the Southern Ocean (Hogg et al., 2015; Martínez-Moreno  
 301 et al., 2021). Furthermore, by analogy the long-term decrease in the number of coher-  
 302 ent eddies and increase in coherent eddy amplitude could be a consequence of a long-  
 303 term increase in the energy cascade, where interactions between eddies have generated  
 304 a stronger coherent eddy field over the satellite record.

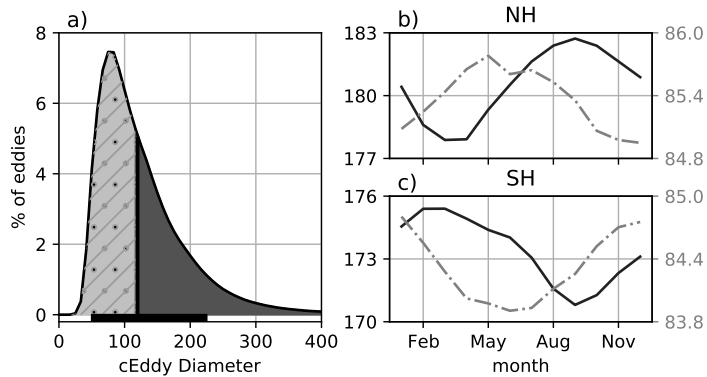
320 The coherent eddy amplitude from positive coherent eddies and negative coherent  
 321 eddies show similar seasonal cycles to the absolute eddy amplitude (Figure 8). However,  
 322 by separating the polarity contribution, its observed that the amplitude of negative co-  
 323 herent eddies in the Northern Hemisphere has decreased (Figure 8b). In the Southern  
 324 Ocean, the increase in absolute eddy amplitude is further corroborated as both coher-  
 325 ent eddy polarities show an increase since the early 90s (Figure 8e,f).

## 335 5 Trends

336 It is expected from the results presented in Figures 4, 6, and 8 a long-term read-  
 337 justment of the coherent eddy field. In particular, we now explore the long-term trends  
 338 in the number of coherent eddies and absolute coherent eddy amplitude using both track-



305 **Figure 6.** Hemispherical seasonality of the coherent eddy statistics; a,e) seasonal cycle of the  
 306 number of coherent eddies ( $cEddy_n$ ); b,f) seasonal cycle of the mean coherent eddy amplitude  
 307 ( $cEddy_{amp}$ ); c,g) seasonal cycle of the warm core coherent eddies amplitude (positive  $cEddy_{amp}$ );  
 308 d,h) seasonal cycle of the cold core coherent eddies amplitude (negative  $cEddy_{amp}$ ). Panels a,b  
 309 and c show the northern hemisphere seasonal cycle, while panels d,e, and f correspond to the  
 310 southern hemisphere. Dashed lines correspond to the seasonal cycle of the fields and dotted lines  
 311 show the seasonal cycle of the wind magnitude smoothed over 120 days (moving average). The  
 312 green and magenta stars show the maximum of the seasonal cycle for each field and the wind  
 313 magnitude, respectively. The line colors show the year.



314 **Figure 7.** Distribution of the identified eddy diameter and hemispherical seasonality of the  
 315 coherent eddy diameter. a) Distribution in percentage of identified eddy amplitude, solid bar bel-  
 316 low distribution represents 90% of the identified eddies. Seasonal cycle of the eddy diameter for  
 317 the b) Northern Hemisphere and c) Southern Hemisphere. Dark solid line and area corresponds  
 318 to coherent eddies with diameters larger than 120 km, while light gray dash-dotted line and area  
 319 shows coherent eddies with diameters smaller than 120 km.

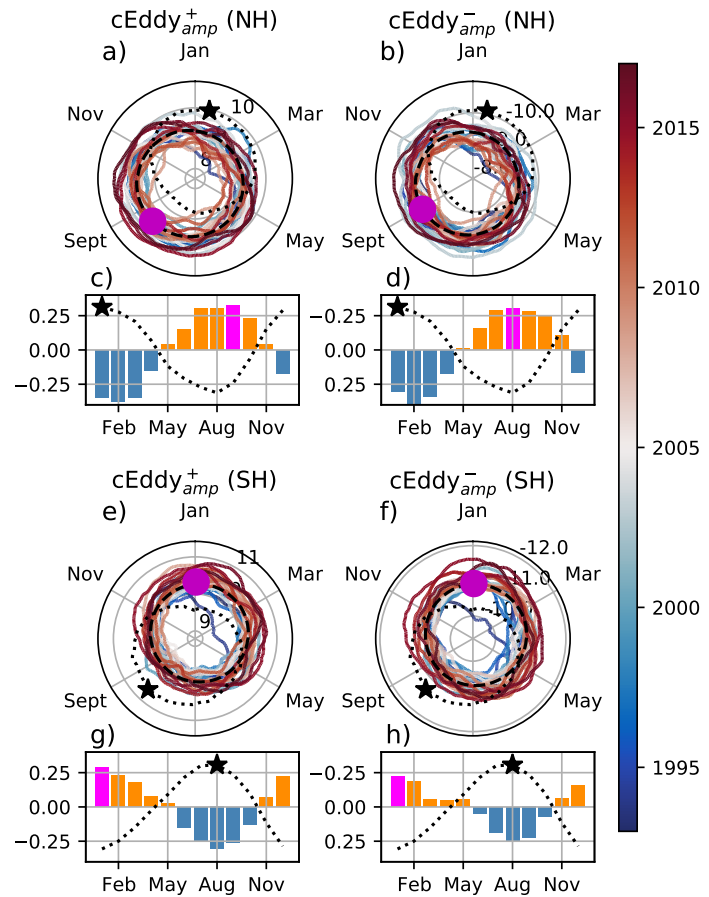
339 ing algorithm datasets (Figure 9). Both datasets show consistent trend and significance  
 340 patterns. Several regions in the ocean, such as the Southern Ocean, North Atlantic and  
 341 North Pacific show a decrease in the number of eddies, meanwhile those same regions  
 342 have a clear increase in the absolute coherent eddy amplitude. This collocation of de-  
 343 crease in number and increase in eddy amplitude further supports an intensification of  
 344 the coherent eddy field though eddy-eddy interactions. These trends are similar to those  
 345 observed in mesoscale eddy kinetic energy (Martínez-Moreno et al., 2021) and provide  
 346 additional evidence of a readjustment of the mesoscale eddy field over the last 3 decades.

## 353 6 Regional

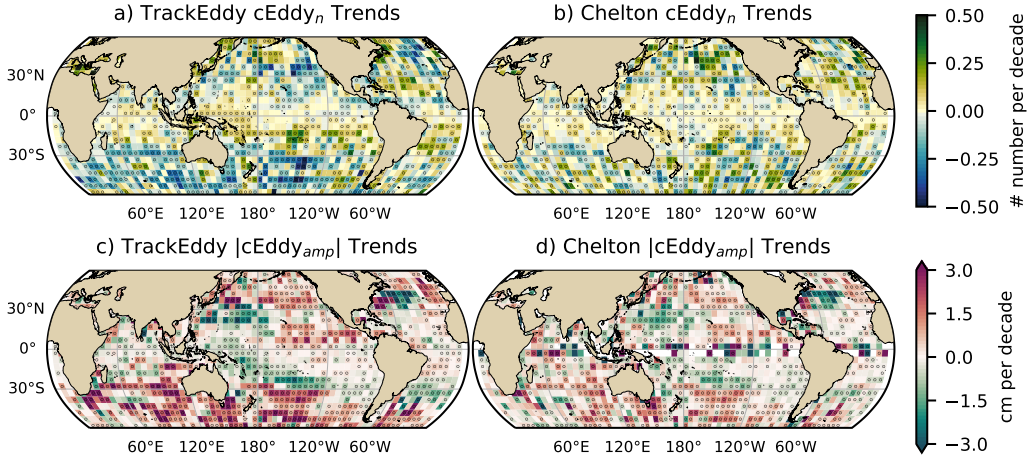
354 For regions with relatively large proportions of CEKE (i.e., boundary currents and  
 355 eastern currents), we investigate the seasonal and long-term variability in individual ocean  
 356 regions.

### 357 6.1 Boundary Currents

358 The most energetic western boundary currents include; the Agulhas Current, the  
 359 Kuroshio Current, and the Gulf Stream (Figures 10, 11, and 12). In all these currents



326 **Figure 8.** Hemispherical seasonality of the coherent eddy statistics; a,e) seasonal cycle of the  
 327 number of coherent eddies ( $cEddy_n$ ); b,f) seasonal cycle of the mean coherent eddy amplitude  
 328 ( $cEddy_{amp}$ ); c,g) seasonal cycle of the warm core coherent eddies amplitude (positive  $cEddy_{amp}^+$ );  
 329 d,h) seasonal cycle of the cold core coherent eddies amplitude (negative  $cEddy_{amp}^-$ ). Panels a,b  
 330 and c show the northern hemisphere seasonal cycle, while panels d,e, and f correspond to the  
 331 southern hemisphere. Dashed lines correspond to the seasonal cycle of the fields and dotted lines  
 332 show the seasonal cycle of the wind magnitude smoothed over 120 days (moving average). The  
 333 green and magenta stars show the maximum of the seasonal cycle for each field and the wind  
 334 magnitude, respectively. The line colors show the year.



347 **Figure 9.** Trends of coherent eddy statistics. a) and b) Trends of the number of identified  
 348 coherent eddies from satellite observations identified using TrackEddy, and those reported in  
 349 Chelton's dataset. c) and e) Trends of the mean absolute value of identified coherent eddies am-  
 350 plitude from satellite observations identified using TrackEddy, and those reported in Chelton's  
 351 dataset. Gray stippling shows regions that are statistically significant above the 95% confidence  
 352 level.

360 without exception and relative to the mean western boundary current location; (i) CEKE  
 361 contains around 80% of the EKE equatorward, (ii) the number of eddies is larger equa-  
 362 torward, and (iii) the absolute eddy amplitude is larger polewards of the mean western  
 363 boundary current location.

364 a large amplitudes

365 **Figure 10**

- 366 • Described similar to figure 7, 8, and 9  
 367 • Note that boundary currents have a consistent seasonal cycle in the positive and  
 368 negative eddy amplitude.  
 369 • As expected, the seasonal cycle is opposite to BC in the northern hemisphere.

370 **Figure 11**

- 371 • Described similar to figure 7, 8, and 9

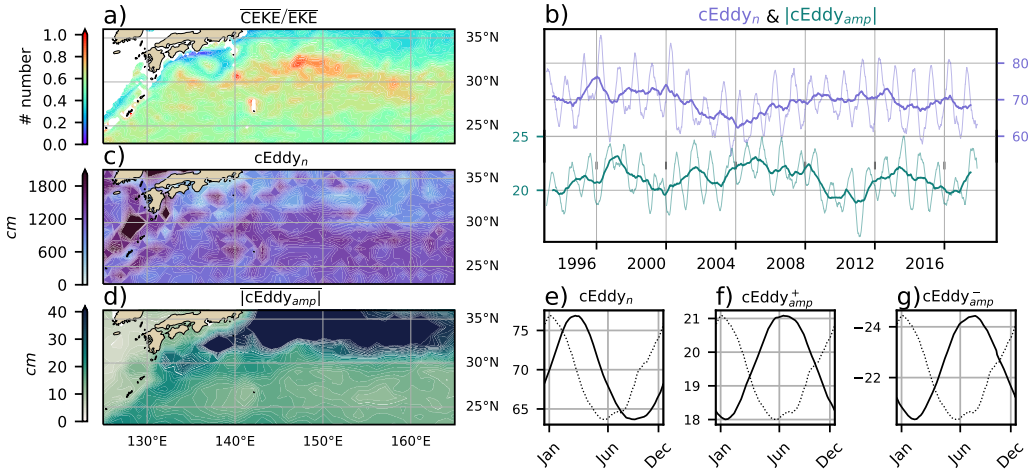


**Figure 10.** Same as Figure 13 but for the Kuroshio Current.

- Note that boundary currents have a consistent seasonal cycle in the positive and negative eddy amplitude.

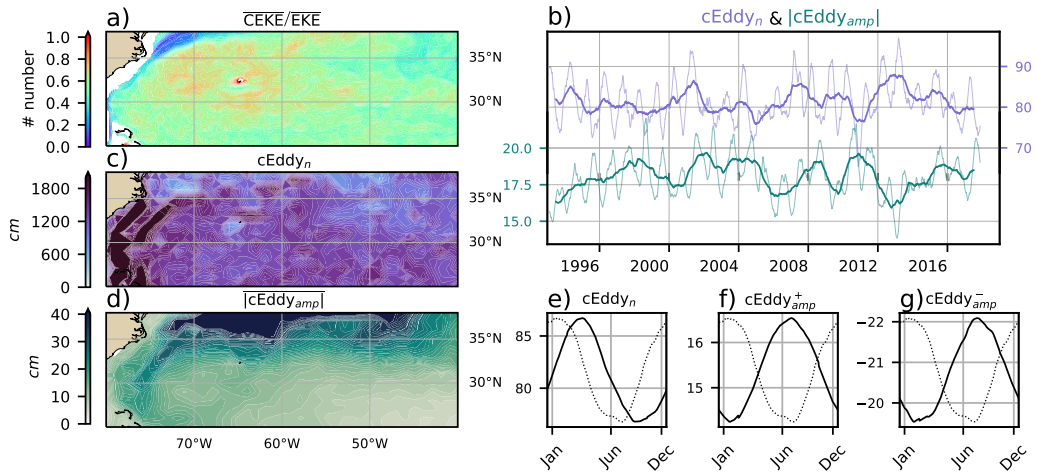
### Figure 12

- Described similar to figure 7, 8, and 9
- Note that boundary currents have a consistent seasonal cycle in the positive and negative eddy amplitude.
- Delete Fig 11 or 12, they are really similar. What do you think?

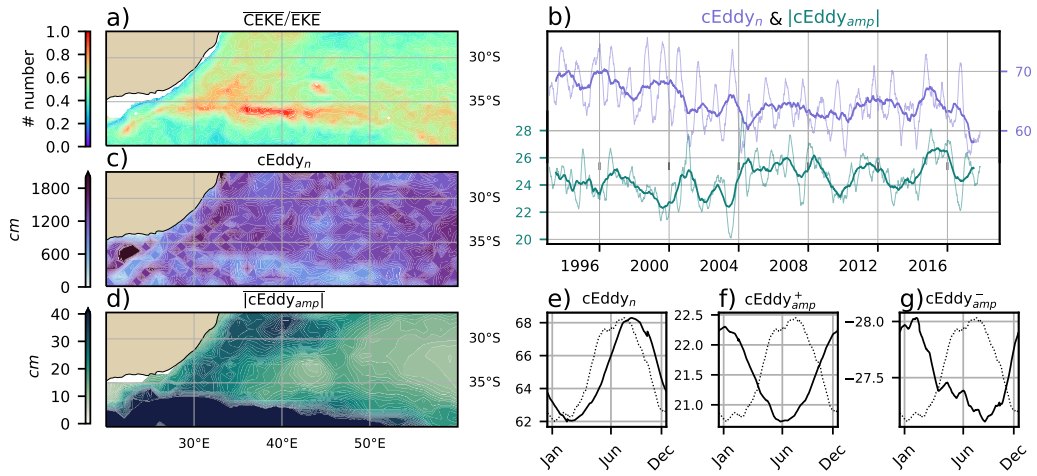
## 6.2 Eastern currents

### Figure 7

- South of the Leeuwin Current there is an important dominance fo the coherent eddy field, where it explains around 80% of the eddy kinetic energy.
- Although this region does not have a large EKE, we can observe a considerable amount of eddies across the region, but more importantly the coherent eddy amplitude is particularly large in those regions with coherent eddy dominance.
- The solid lines show an decrease in the number of eddies, but an increase in the eddy amplitude.
- Moreover, the coherent eddy number peaks in August.

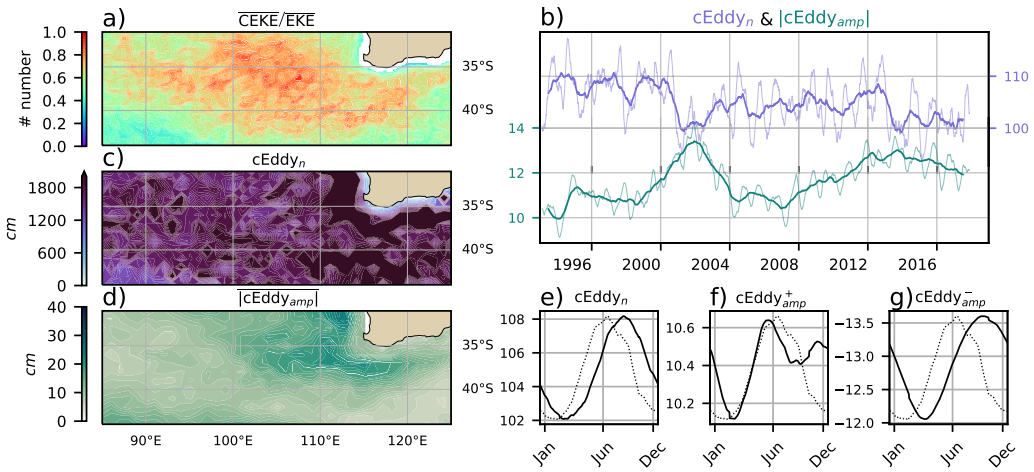


380

**Figure 11.** Move to supplementary Same as Figure 13 but for the Gulf Stream.

381

**Figure 12.** Same as Figure 13 but for the Agulhas Current.



396 **Figure 13.** Climatology of the eddy field and coherent eddy field at the Leeuwin Current. a)  
 397 Ratio of mean coherent eddy kinetic energy ( $\overline{\text{CEKE}}$ ) versus mean eddy kinetic energy ( $\overline{\text{EKE}}$ ); b)  
 398 Thick lines show the running average over 2 years and thin lines show the running average over  
 399 90 days of the coherent eddy number sum and the average absolute coherent eddy amplitude; c)  
 400 Map of the number of eddies; d) Map of the average absolute coherent eddy amplitude; e) Sea-  
 401 sonal cycle of the number of eddies f) Seasonal cycle of the positive coherent eddy amplitude. g)  
 402 Seasonal cycle of the negative coherent eddy amplitude.

- 392 Meanwhile coherent eddies with the positive amplitude have a smaller amplitude  
 393 than the negative, furthermore, the positive eddies peak in Jun and show a inter-  
 394 annual modulation, while the negative eddies peak in October.
- 395 • Research regional dynamics (Add here why we may expect this response.)

### 403 **Figure 9**

- 404 • Here we observe that the number of eddies and eddy amplitude are large in the  
 405 area where the coherent eddies dominate the eddy field.
- 406 • Dynamically, in this region eddies are generated due to Rossby wave propagation  
 407 along the coast that becomes unstable and sheds eddies at the Tehuantepec Gulf.
- 408 • The seasonal cycle shows a peak in Jun, while the positive amplitude is observed  
 409 in March and the negative amplitude maximum occurs in September.
- 410 • Research regional dynamics (Add here why we may expect this response.)

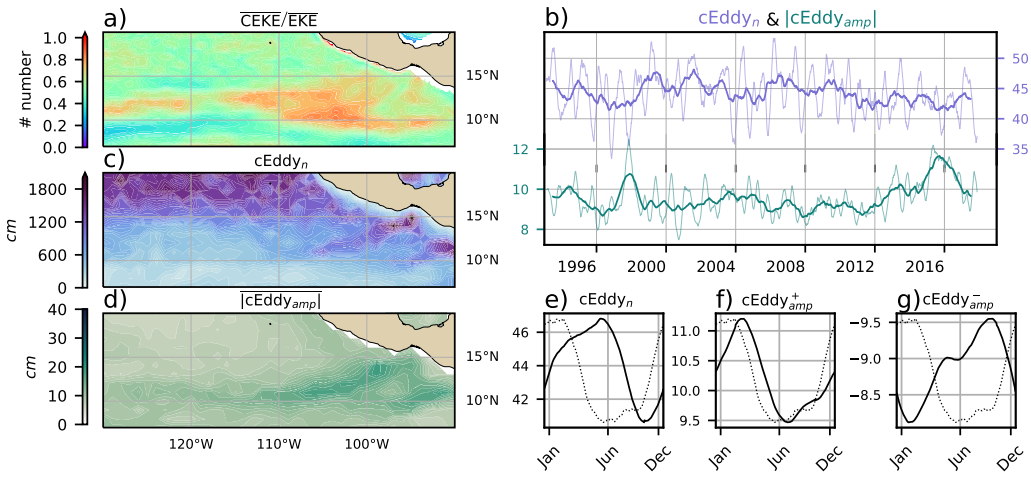


**Figure 14.** Same as Figure 13 but for the East Tropical Pacific.

411

## 7 Summary and Conclusions

412

### Acknowledgments

413  
414  
415  
416  
417  
418  
419  
420  
421  
422

Chelton & Schlax (2013) dataset was produced by SSALTO/DUACS and distributed by AVISO+ (<https://www.aviso.altimetry.fr/>) with support from CNES, developed and validated in collaboration with E.Mason at IMEDEA. Global coherent eddy reconstruction, coherent and non-coherent eddy kinetic energy datasets, in addition to gridded coherent eddy tracking datasets are publicly available at (<https://doi.org/10.5281/zenodo.4646429>). All analyses and figures in this manuscript are reproducible via Jupyter notebooks and instructions can be found in the Github repository `CEKE_climatology` ([https://github.com/josuemtzmo/CEKE\\_climatology](https://github.com/josuemtzmo/CEKE_climatology)). Trends used the Python Package `xarrayMannKendall` (<https://doi.org/10.5281/zenodo.4458776>)

423

### References

424  
425  
426  
427  
428  
429

- Arbic, B. K., Polzin, K. L., Scott, R. B., Richman, J. G., & Shriver, J. F. (2013). On Eddy Viscosity, Energy Cascades, and the Horizontal Resolution of Gridded Satellite Altimeter Products\*. *Journal of Physical Oceanography*, 43(2), 283–300. doi: 10.1175/jpo-d-11-0240.1
- Ashkezari, M. D., Hill, C. N., Follett, C. N., Forget, G., & Follows, M. J. (2016). Oceanic eddy detection and lifetime forecast using machine learning methods.

- 430                   *Geophysical Research Letters*, 43(23). doi: 10.1002/2016gl071269
- 431                   Beron-Vera, F. J., Wang, Y., Olascoaga, M. J., Goni, G. J., & Haller, G. (2013). Ob-  
432                   jective Detection of Oceanic Eddies and the Agulhas Leakage. *Journal of Physical*  
433                   *Oceanography*, 43(7), 1426–1438. doi: 10.1175/JPO-D-12-0171.1
- 434                   Bouali, M., Sato, O. T., & Polito, P. S. (2017). Temporal trends in sea surface tem-  
435                   perature gradients in the South Atlantic Ocean. *Remote Sensing of Environment*,  
436                   194, 100–114. doi: 10.1016/j.rse.2017.03.008
- 437                   Callies, J., Flierl, G., Ferrari, R., & Fox-Kemper, B. (2015). The role of mixed-layer  
438                   instabilities in submesoscale turbulence. *Journal of Fluid Mechanics*, 788, 5–41.  
439                   doi: 10.1017/jfm.2015.700
- 440                   Cane, M. A., Clement, A. C., Kaplan, A., Kushnir, Y., Pozdnyakov, D., Seager, R.,  
441                   ... Murtugudde, R. (1997). Twentieth-Century Sea Surface Temperature Trends.  
442                   *Science*, 275(5302), 957–960. doi: 10.1126/science.275.5302.957
- 443                   Chelton, D. B., Gaube, P., Schlax, M. G., Early, J. J., & Samelson, R. M. (2011).  
444                   The influence of nonlinear mesoscale eddies on near-surface oceanic chlorophyll.  
445                   *Science*, 334(6054), 328–32. doi: 10.1126/science.1208897
- 446                   Chelton, D. B., & Schlax, M. G. (2013). *Mesoscale eddies in altimeter observations*  
447                   of ssh.
- 448                   Chelton, D. B., Schlax, M. G., Samelson, R. M., & de Szoeke, R. A. (2007). Global  
449                   observations of large oceanic eddies. *Geophysical Research Letters*, 34(15),  
450                   L15606. doi: 10.1029/2007GL030812
- 451                   CMEMS. (2017). The Ssalto/Duacs altimeter products were produced and dis-  
452                   tributed by the Copernicus Marine and Environment Monitoring Service. *Aviso*  
453                   Dataset. Retrieved from <https://www.aviso.altimetry.fr/>
- 454                   Cui, W., Wang, W., Zhang, J., & Yang, J. (2020). Identification and census statis-  
455                   tics of multicore eddies based on sea surface height data in global oceans. *Acta*  
456                   *Oceanologica Sinica*, 39(1), 41–51. doi: 10.1007/s13131-019-1519-y
- 457                   Faghmous, J. H., Frenger, I., Yao, Y., Warmka, R., Lindell, A., & Kumar, V. (2015,  
458                   6). A daily global mesoscale ocean eddy dataset from satellite altimetry. *Scientific*  
459                   *Data*, 2, 150028 EP -. doi: 10.1038/sdata.2015.28
- 460                   Ferrari, R., & Wunsch, C. (2009). Ocean Circulation Kinetic Energy: Reservoirs,  
461                   Sources, and Sinks. *Annual Review of Fluid Mechanics*, 41(1), 253–282. doi: 10  
462                   .1146/annurev.fluid.40.111406.102139

- 463 Frenger, I., Gruber, N., Knutti, R., & Münnich, M. (2013). Imprint of Southern  
464 Ocean eddies on winds, clouds and rainfall. *Nature Geoscience*, 6(8), 608 EP -.  
465 doi: 10.1038/ngeo1863
- 466 Frenger, I., Münnich, M., Gruber, N., & Knutti, R. (2015). Southern Ocean eddy  
467 phenomenology. *Journal of Geophysical Research: Oceans*, 120(11), 7413-7449.  
468 doi: 10.1002/2015JC011047
- 469 Fu, L., Chelton, D., Le Traon, P., & Oceanography, M. R. (2010). Eddy dynamics  
470 from satellite altimetry. *Oceanography*, 23(4), 14-25. doi: 10.2307/24860859
- 471 Gill, A., Green, J., & Simmons, A. (1974). Energy partition in the large-scale ocean  
472 circulation and the production of mid-ocean eddies. *Deep Sea Res Oceanogr Abstr*,  
473 21(7), 499-528. doi: 10.1016/0011-7471(74)90010-2
- 474 Hogg, A. M., & Blundell, J. R. (2006). Interdecadal variability of the southern  
475 ocean. *Journal of Physical Oceanography*, 36(8), 1626-1645. doi: 10.1175/  
476 JPO2934.1
- 477 Hogg, A. M., Meredith, M. P., Chambers, D. P., Abrahamsen, E. P., Hughes,  
478 C. W., & Morrison, A. K. (2015). Recent trends in the Southern Ocean  
479 eddy field. *Journal of Geophysical Research: Oceans*, 120(1), 257-267. doi:  
480 10.1002/2014JC010470
- 481 Hu, S., Sprintall, J., Guan, C., McPhaden, M. J., Wang, F., Hu, D., & Cai,  
482 W. (2020, 2). Deep-reaching acceleration of global mean ocean circula-  
483 tion over the past two decades. *Science Advances*, 6(6), eaax7727. doi:  
484 10.1126/sciadv.aax7727
- 485 Japan Meteorological Agency, Japan. (2013). *Jra-55: Japanese 55-year reanalysis*,  
486 *daily 3-hourly and 6-hourly data*. Boulder CO: Research Data Archive at the Na-  
487 tional Center for Atmospheric Research, Computational and Information Systems  
488 Laboratory. Retrieved from <https://doi.org/10.5065/D6HH6H41>
- 489 Kang, D., & Curchitser, E. N. (2017). On the Evaluation of Seasonal Variability of  
490 the Ocean Kinetic Energy. *Geophysical Research Letters*, 47, 1675-1583. doi: 10  
491 .1175/JPO-D-17-0063.1
- 492 Li, G., Cheng, L., Zhu, J., Trenberth, K. E., Mann, M. E., & Abraham, J. P. (2020).  
493 Increasing ocean stratification over the past half-century. *Nature Climate Change*,  
494 1-8. doi: 10.1038/s41558-020-00918-2
- 495 Martínez-Moreno, J., Hogg, A. M., England, M., Constantinou, N. C., Kiss, A. E.,

- 496 & Morrison, A. K. (2021). Global changes in oceanic mesoscale currents over the  
497 satellite altimetry record. *Journal of Advances in Modeling Earth Systems*, 0(ja).  
498 doi: 10.1029/2019MS001769
- 499 Martínez-Moreno, J., Hogg, A. M., Kiss, A. E., Constantinou, N. C., & Morrison,  
500 A. K. (2019). Kinetic energy of eddy-like features from sea surface altimeter.  
501 *Journal of Advances in Modeling Earth Systems*, 11(10), 3090-3105. doi:  
502 10.1029/2019MS001769
- 503 Patel, R. S., Llort, J., Strutton, P. G., Phillips, H. E., Moreau, S., Pardo, P. C.,  
504 & Lenton, A. (2020). The Biogeochemical Structure of Southern Ocean  
505 Mesoscale Eddies. *Journal of Geophysical Research: Oceans*, 125(8). doi:  
506 10.1029/2020jc016115
- 507 Pilo, G. S., Mata, M. M., & Azevedo, J. L. L. (2015). Eddy surface properties and  
508 propagation at Southern Hemisphere western boundary current systems. *Ocean  
509 Science*, 11(4), 629–641. doi: 10.5194/os-11-629-2015
- 510 Qiu, B. (1999). Seasonal Eddy Field Modulation of the North Pacific Subtropical  
511 Countercurrent: TOPEX/Poseidon Observations and Theory. *Journal of Physical  
512 Oceanography*, 29(10), 2471–2486. doi: 10.1175/1520-0485(1999)029<2471:sefmot>2  
513 .0.co;2
- 514 Qiu, B., & Chen, S. (2004). Seasonal Modulations in the Eddy Field of the South  
515 Pacific Ocean. *Journal of Physical Oceanography*, 34(7), 1515–1527. doi: 10.1175/  
516 1520-0485(2004)034<1515:smitef>2.0.co;2
- 517 Qiu, B., Chen, S., Klein, P., Sasaki, H., & Sasai, Y. (2014). Seasonal Mesoscale  
518 and Submesoscale Eddy Variability along the North Pacific Subtropical Coun-  
519 tercurrent. *Journal of Physical Oceanography*, 44(12), 3079–3098. doi:  
520 10.1175/JPO-D-14-0071.1
- 521 Ruela, R., Sousa, M. C., deCastro, M., & Dias, J. M. (2020). Global and regional  
522 evolution of sea surface temperature under climate change. *Global and Planetary  
523 Change*, 190, 103190. doi: 10.1016/j.gloplacha.2020.103190
- 524 Sasaki, H., Klein, P., Qiu, B., & Sasai, Y. (2014). Impact of oceanic-scale inter-  
525 actions on the seasonal modulation of ocean dynamics by the atmosphere. *Nature  
526 Communications*, 5(1), 5636. doi: 10.1038/ncomms6636
- 527 Schubert, R., Schwarzkopf, F. U., Baschek, B., & Biastoch, A. (2019). Submesoscale  
528 Impacts on Mesoscale Agulhas Dynamics. *Journal of Advances in Modeling Earth*

- 529                   *Systems*, 11(8), 2745–2767. doi: 10.1029/2019ms001724
- 530                   Siegel, D., Peterson, P., DJ, M., Maritorena, S., & Nelson, N. (2011). Bio-optical  
531                   footprints created by mesoscale eddies in the Sargasso Sea. *Geophysical Research  
532                   Letters*, 38(13), n/a-n/a. doi: 10.1029/2011GL047660
- 533                   Uchida, T., Abernathey, R., & Smith, S. (2017). Seasonality of eddy kinetic energy  
534                   in an eddy permitting global climate model. *Ocean Modelling*, 118, 41-58. doi: 10  
535                   .1016/j.ocemod.2017.08.006
- 536                   Wunsch, C. (2020). Is The Ocean Speeding Up? Ocean Surface Energy Trends.  
537                   *Journal of Physical Oceanography*, 50(11), 1–45. doi: 10.1175/jpo-d-20-0082.1
- 538                   Wunsch, C., & Ferrari, R. (2004). Vertical mixing, energy, and the general circula-  
539                   tion of the oceans. *Annual Review of Fluid Mechanics*, 36(1), 281–314. doi: 10  
540                   .1146/annurev.fluid.36.050802.122121
- 541                   Wyrtki, K., Magaard, L., & Hager, J. (1976). Eddy energy in the oceans. *Journal of  
542                   Geophysical Research*, 81(15), 2641-2646. doi: 10.1029/JC081i015p02641
- 543                   Yue, S., & Wang, C. (2004). The Mann-Kendall Test Modified by Effective Sample  
544                   Size to Detect Trend in Serially Correlated Hydrological Series. *Water Resources  
545                   Management*, 18(3), 201–218. doi: 10.1023/b:warm.0000043140.61082.60